Electronic Supplementary Information

Highly Pressure-Sensitive, Hydrophobic, and Flexible 3D Carbon Nanofiber Networks by Electrospinning for Human Physiological Signals Monitoring

Zhiyuan Han,[a,b] *Zhiqiang Cheng,*[c] *Ying Chen,*[d] *Bo Li,* [d] *Ziwei Liang,*[a,b] *Hangfei Li,*[a,b] *Yinji Ma,*[a,b] *and Xue Feng*[a,b]

a. AML, Department of Engineering Mechanics, Tsinghua University, Beijing, 100084, China

b. Center for Flexible Electronics Technology, Tsinghua University, Beijing, 100084, China

c. College of Resources and Environment, Jilin Agriculture University, Changchun, 130118, China

d. Institute of Flexible Electronics Technology of THU, Zhejiang, Jiaxing, 314000, China

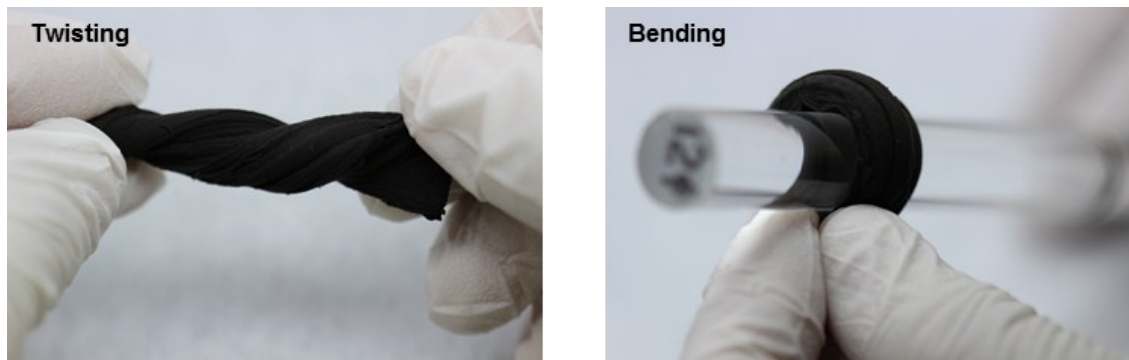*To whom correspondence should be addressed.
*E-mail: fengxue@tsinghua.edu.cn

Fig. S1. Photographs showing the excellent flexibility of CNFNs during twisting and bending.
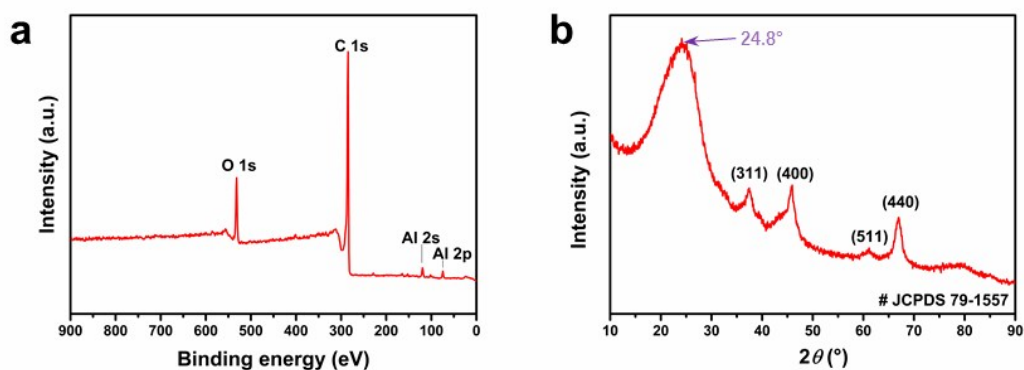

Fig. S2. (a) Wide-scan XPS survey spectroscopy of the CNFNs. The main peaks presenting in the spectrum are from O, C, and Al. (b) X-ray diffraction pattern of CNFNs. The XRD pattern has a strong peak at $2\theta=24.8°$, indicating a high graphitization degree. The pattern has sharp peaks at $2\theta=37.7°$, $45.8°$, $60.8°$, and $66.8°$,which is attributed to the (311), (400), (511), and (440) reflection of Al_2O_3.
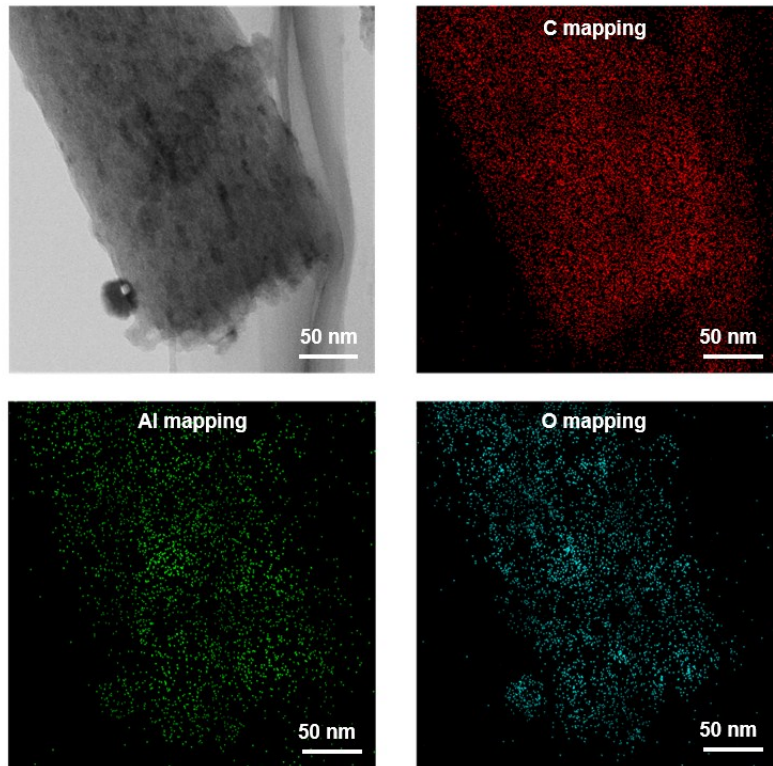
Fig. S3. TEM image and corresponding elemental mapping images of the CNFNs surface, which indicates that Al_2O_3 is evenly distributed in the fibers.
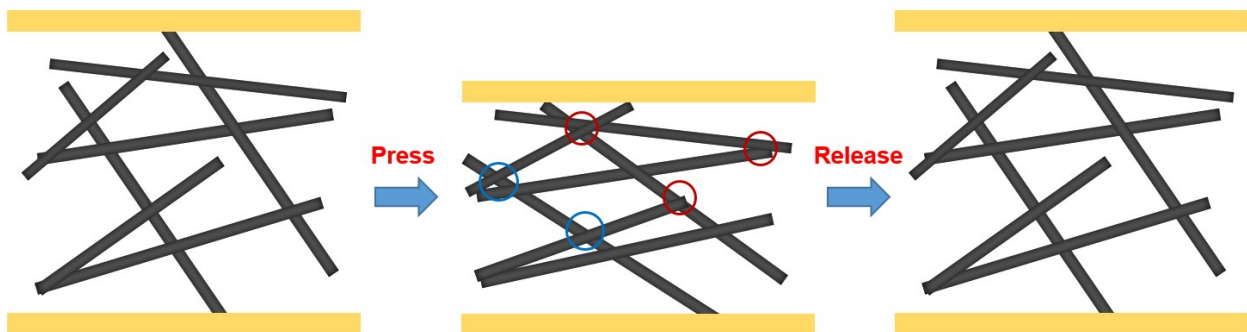

Fig. S4. Schematic illustration of the piezoresistive sensing of the CNFNs. When the pressure was applied on the CNFNs, the tangled carbon nanofibers make more contact points with each other and the contact area of the fiber network increased a lot, thus leading to the decrease in resistance of the CNFNs.
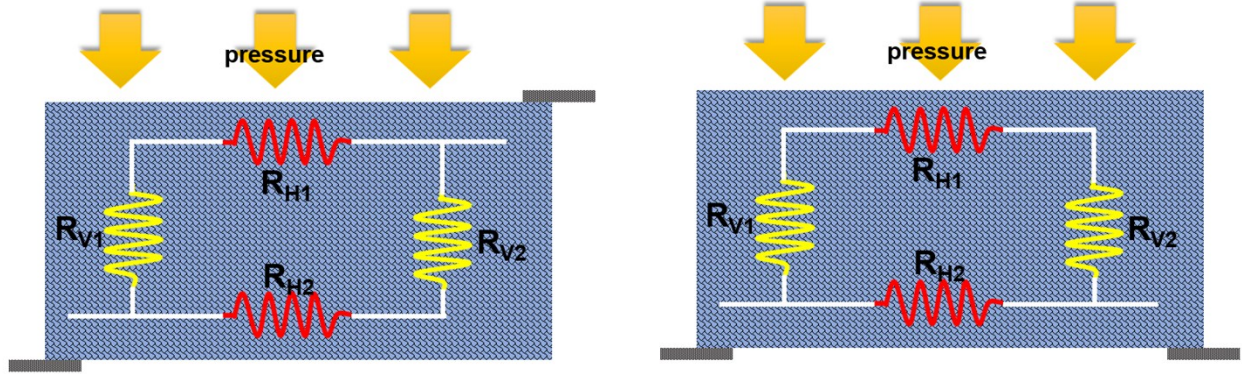
Fig. S5. Two equivalent circuit models for the sample with opposite-surface electrodes and coplanar electrodes, respectively. When the pressure is applied on the surface of the samples, the contact resistance (R_{V1}, R_{V2}) of tangled nanofibers in vertical direction decreases and the contact resistance (R_{H1}, R_{H2}) in horizontal direction is almost constant.

The total resistance for the sample with opposite-surface electrodes: $R_o = \dfrac{(R_{V1} + R_{H1})(R_{V2} + R_{H2})}{R_{V1} + R_{V2} + R_{H1} + R_{H2}}$

The total resistance for the sample with coplanar electrodes: $R_c = \dfrac{(R_{V1} + R_{H1} + R_{V2})R_{H2}}{R_{V1} + R_{V2} + R_{H1} + R_{H2}}$

To obtain a clear analytical solution, we made some simplifications and assumptions: 1. $R_{V1}=R_{V2}=R_V$, $R_{H1}= R_{H2}= R_H$; 2. When pressure was applied, the R_V changed to ($R_V-\Delta R_V$) and the R_V remained unchanged. Under the sample pressure, the resistance variation ratios for these two designs were $\dfrac{\Delta R_o}{R_{o0}} = \dfrac{2\Delta R_V}{R_V + R_H}$ and $\dfrac{\Delta R_c}{R_{c0}} = \dfrac{2\Delta R_V}{2R_V + R_H}$. Therefore, the resistance responses for the two types are different from each other and the pressure sensitivity of the sample with opposite-surface electrodes is larger than that of the sample with coplanar electrodes.
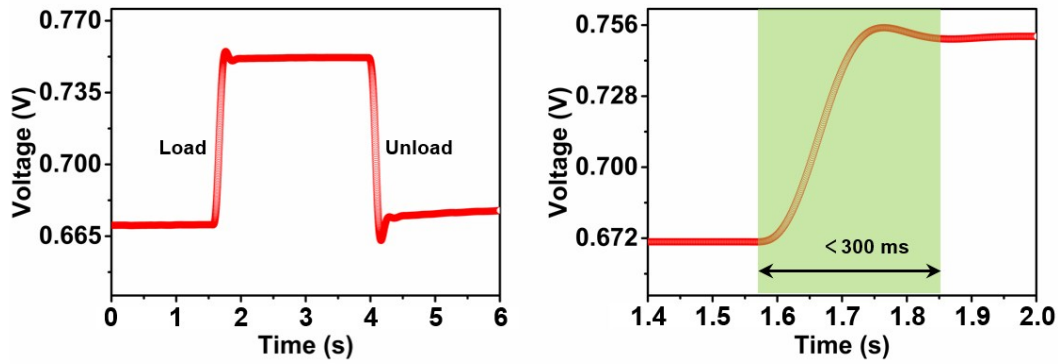
Fig. S6. Real-time response of the CNFNs upon loading pressure and unloading, which demonstrates response time of less than 300 ms. The right Fig. shows the magnified curve of the left one. Note that a voltage acquisition card (NI USB-4431) is used in order to get the high-resolution signals.
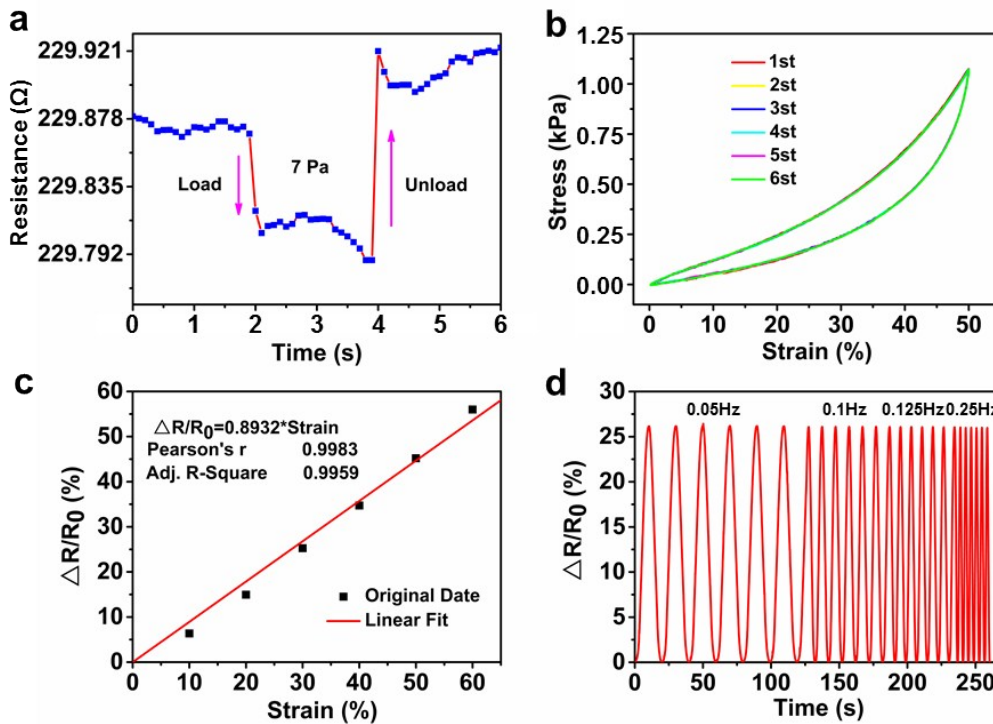

Fig. S7. (a) Detection limit of the CNFNs, which shows resistance variation under subtle pressure of 7 Pa loading and unloading. (b) Stress-strain curves of CNFNs under six periodic loading-unloading tests, which are completely coincident. (c) The resistance variation ratios

versus strain showing excellent linearity. (d) Relative resistance variation of the CNFNs under cyclic loading-unloading with a strain of 25% at different applied frequency (0.05 Hz, 0.1 Hz, 0.124 Hz, and 0.25 Hz), indicating that the resistance response is independent of loading rate.
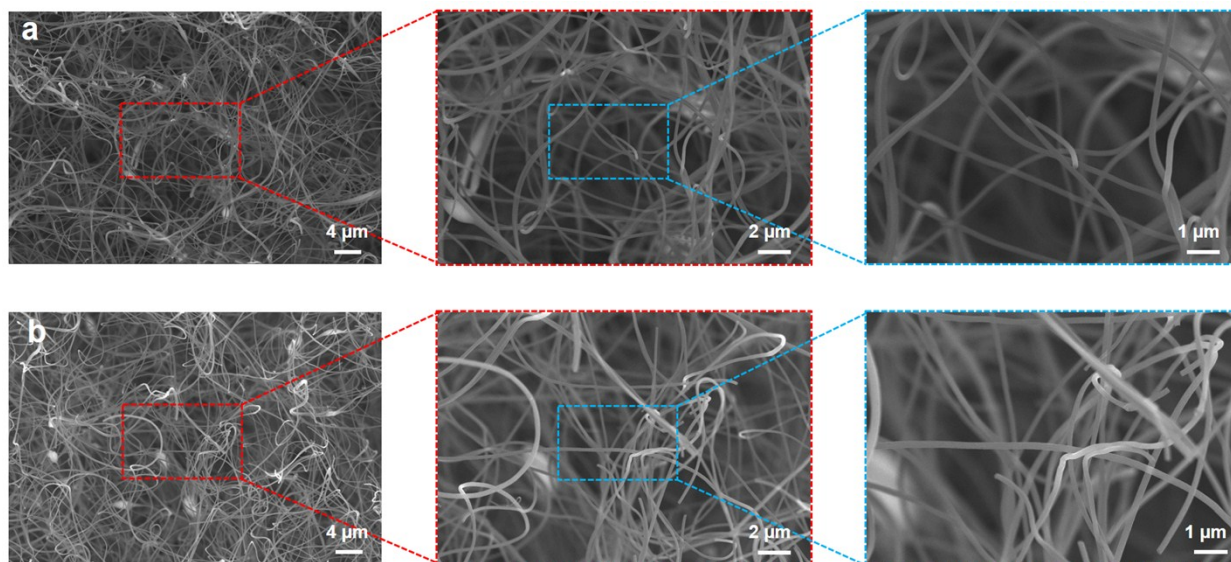

Fig. S8. The morphology of the CNFNs before (a) and after (b) cycling test. No significant changes were found about the structure of the sample.
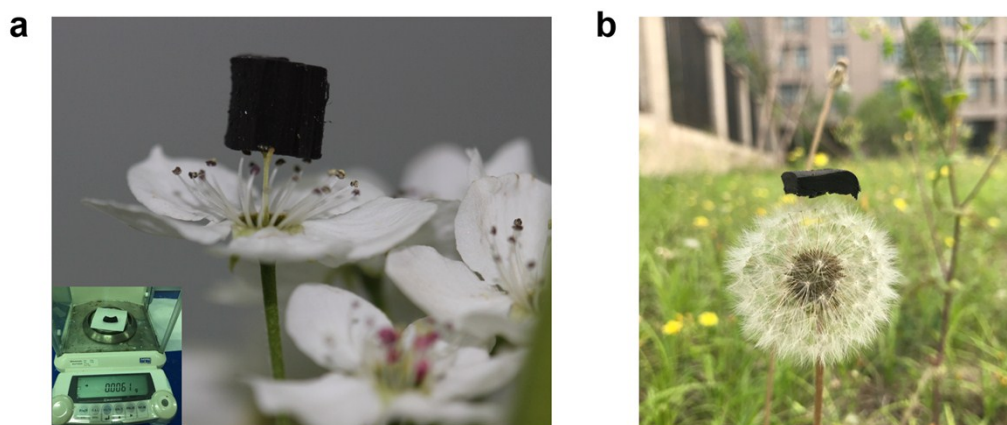

Fig. S9. (a,b) Ultralight CNFNs standing on the tip of flower stamen stably and on the dandelion stably.

Fig. S10. Photograph of emissivity meter, exhibiting a low infrared emissivity of 0.62.
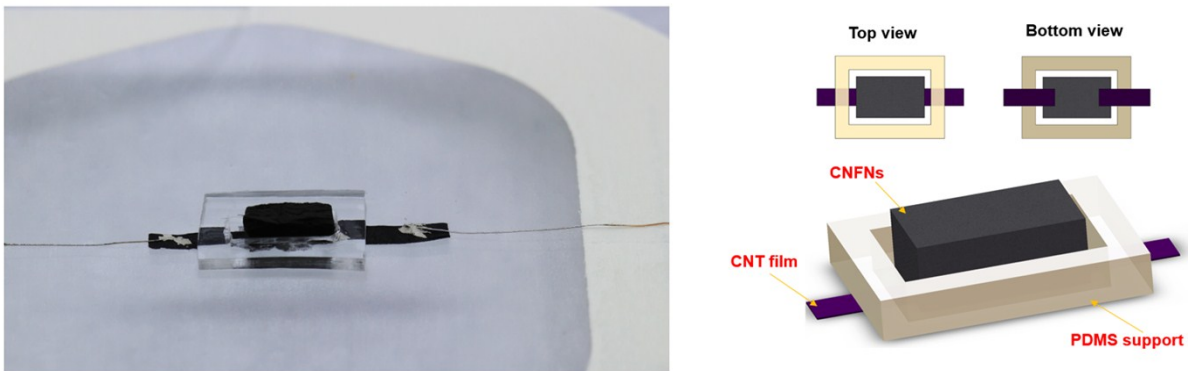

Fig. S11. The schematic illustration of the CNFNs pressure sensor surrounded by the PDMS support. The shape of the PDMS support is a rectangular parallelepiped with a rectangular through hole.
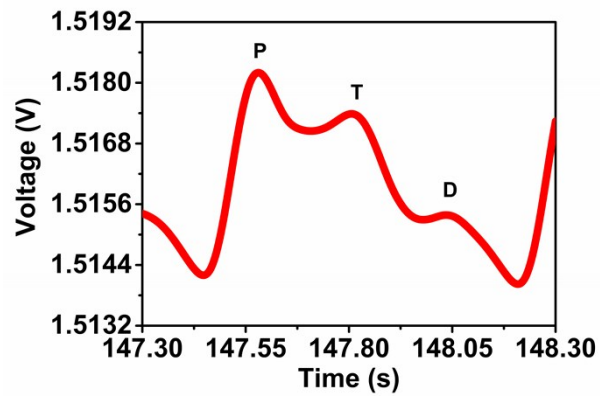
Fig. S12. Zoomed waveform of a typical pulse wave extracted from the original signal, among which the percussion wave (P-wave), tidal wave (T-wave), and diastolic wave (D-wave) are clearly observed.

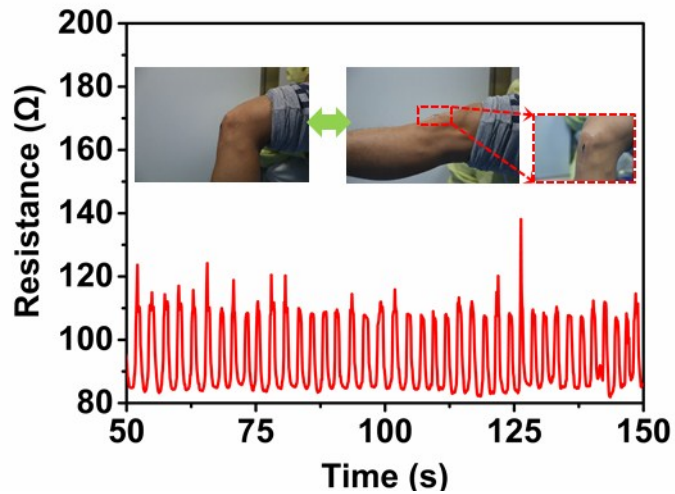**Fig. S13.** The resistance change of the CNFNs sensor in knee bending test, exhibiting excellent repeatability.
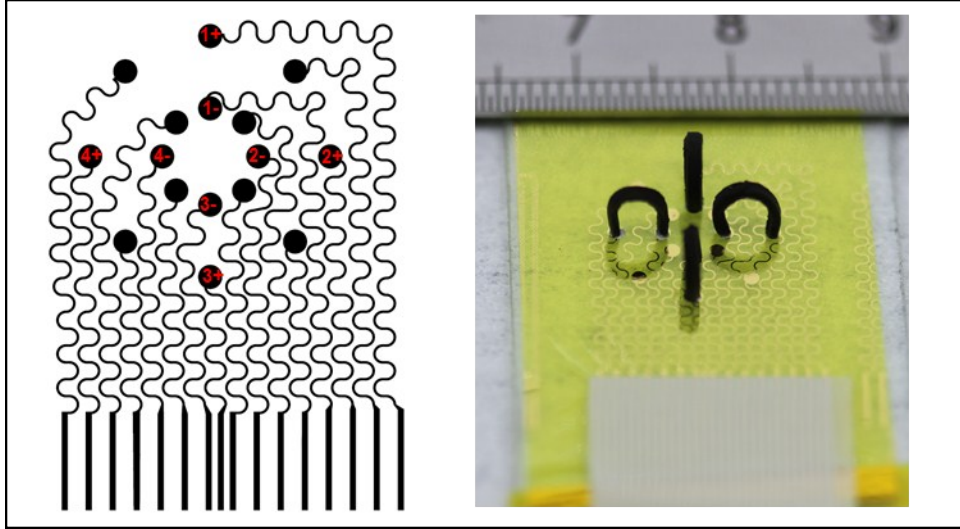
Fig. S14. The electrode geometrical shape of the arch-array sensor platform and the corresponding numbers of the prism CNFNs units.

Table S1. Comparison of pressure sensitivity and other versatile properties of various 3D porous network materials.

Materials	Sensitivity (kPa^{-1})	Density ($mg\ cm^{-3}$)	Thermal conductivity ($mW\ m^{-1}\ K^{-1}$)	Hydrophobicity	Infrared emissivity	Cycle resilience	Compressibility	Flexibility	Ref.
CNFNs	1.41 (highest)	3.6	24	√	0.62	√	>95%	√	This work
Carbon black sponge	0.068	-	-	-	-	√	60%	√	S1
RGO-PU sponge	0.26	-	-	-	-	√	45%	√	S2
KGM based CNFAs	1.02	0.14	-	-	-	√	80%	√	S3
rGO/PI foam	0.18	10	-	-	-	√	50%	√	S4
CNTs/GO@PDMS	0.31	-	-	√	-	√	-	√	S5
CNT sponge	-	1-50	-	-	-	-	80%	√	S6
C-CNC/rGO	-	2.51-3.98	-	-	-	√	99%	√	S7
FIBER NFAs	-	0.12	26	√	-	√	80%	-	S8
rGO composite foam	-	9.2	9	√	-	√	50%	√	S9
TiO_2 sponge	-	8-40	27	-	-	√	50%	-	S10

Supplementary References

S1. X. Wu, Y. Han, X. Zhang, Z. Zhou and C. Lu, *Adv. Funct. Mater.*, 2016, **26**, 6246-6256.

S2. H. B. Yao, J. Ge, C. F. Wang, X. Wang, W. Hu, Z. J. Zheng, Y. Ni and S. H. Yu, *Adv. Mater.*, 2013, **25**, 6692-6698.

S3. Y. Si, X. Wang, C. Yan, L. Yang, J. Yu and B. Ding, *Adv. Mater.*, 2016, **28**, 9512-9518.

S4. Y. Qin, Q. Peng, Y. Ding, Z. Lin, C. Wang, Y. Li, F. Xu, J. Li, Y. Yuan and X. He, *ACS Nano*, 2015, **9**, 8933-8941.

S5. C. Mu, Y. Song, W. Huang, A. Ran, R. Sun, W. Xie and H. Zhang, *Adv. Funct. Mater.*, 2018, **28**, 1707503.

S6. S. Luo, Y. Luo, H. Wu, M. Li, L. Yan, K. Jiang, L. Liu, Q. Li, S. Fan and J. Wang, *Adv. Mater.*, 2017, **29**, 1603549.

S7. H. Zhuo, Y. Hu, X. Tong, Z. Chen, L. Zhong, H. Lai, L. Liu, S. Jing, Q. Liu and C. Liu, *Adv. Mater.*, 2018, **30**, 1706705.

S8. Y. Si, J. Yu, X. Tang, J. Ge and B. Ding, *Nat. Commun.*, 2014, **5**, 5802.

S9. Q. Peng, Y. Qin, X. Zhao, X. Sun, Q. Chen, F. Xu, Z. Lin, Y. Yuan, Y. Li and J. Li, *ACS Appl. Mater. Interfaces*, 2017, **9**, 44010-44017.

S10. H. Wang, X. Zhang, N. Wang, Y. Li, X. Feng, Y. Huang, C. Zhao, Z. Liu, M. Fang and G. Ou, *Sci. Adv.*, 2017, **3**, e1603170.

Supplementary Movie Captions

Movie S1. Demonstration of super compressibility (>95%) of the CNFNs.

Movie S2. Real-time cycling test of the CNFNs.

Movie S3. Demonstration of the CNFNs floating like a feather.

Movie S4. Real-time of the direction identification of tangential forces.